

# Galaxy clustering in a new implementation of the GAEA semi-analytical galaxy formation model

Fabio Fontanot<sup>1,2,\*</sup>, Gabriella De Lucia<sup>1,2</sup>, Lizhi Xie<sup>3</sup>, Michaela Hirschmann<sup>4,1</sup>, Carlton Baugh<sup>5,6</sup>, and John C. Helly<sup>5</sup>

<sup>1</sup> INAF - Astronomical Observatory of Trieste, via G.B. Tiepolo 11, I-34143 Trieste, Italy

<sup>2</sup> IFPU - Institute for Fundamental Physics of the Universe, via Beirut 2, 34151, Trieste, Italy

<sup>3</sup> Tianjin Astrophysics Center, Tianjin Normal University, Binshuixidao 393, 300384, Tianjin, China

<sup>4</sup> EPFL - Institute for Physics, Laboratory for Galaxy Evolution, Observatoire de Sauverny, Chemin Pegasi 51, 1290 Versoix, CH

<sup>5</sup> ICC - Institute for Computational Cosmology, Department of Physics, Durham University, South Road, Durham DH1 3LE, UK

<sup>6</sup> Institute for Data Science, Durham University, South Road, Durham DH1 3LE, UK

Received ???, 2024; accepted ???, 2024

## ABSTRACT

We present results from the latest version of the GALaxy Evolution and Assembly (GAEA) theoretical model of galaxy formation coupled with merger trees extracted from the P-Millennium Simulation (PMS). With respect to the Millennium Simulation, typically adopted in our previous work, the PMS provides a better mass resolution ( $\sim 10^8 h^{-1} M_\odot$ ), a larger volume ( $800^3 \text{ Mpc}^3$ ) and assumes cosmological parameters consistent with latest results from the Planck mission. The model includes, at the same time, a treatment for the partition of cold gas into atomic and molecular ( $\text{H}_2$ ) components; a better treatment for environmental processes acting on satellite galaxies; an updated modelling of cold gas accretion on Super-Massive Black Hole, leading to the Active Galactic Nuclei (AGN) phenomenon and relative feedback on the host galaxy. We compare GAEA predictions based on the PMS, with model realizations based on other simulations in the Millennium Suite at different resolution, showing that the new model provides a remarkable consistency in most statistical properties of galaxy populations. We interpret this as due to the interplay between AGN feedback and  $\text{H}_2$ -based SFR (both acting as regulators of the cold gas content in model galaxies), as model version considering only one of the two mechanisms do not show the same level of consistency in the predictions. We then compare model predictions with available data for the galaxy 2-point correlation function (2pCF) in the redshift range  $0 < z \lesssim 3$ . We show that GAEA runs are able to correctly recover the main dependencies of the 2pCF as a function of stellar mass ( $M_*$ ), star formation activity, HI-content and redshift for  $M_* < 10^{11} M_\odot$  galaxies. These results suggest that our model correctly captures both the distribution of galaxy populations in the Large Scale Structure and the interplay between the main physical processes regulating their baryonic content, both for central and satellite galaxies. At larger stellar masses GAEA underpredicts the 2pCF amplitude, suggesting that model massive galaxies live in less massive dark matter haloes. The model predicts a rather small redshift evolution of the clustering amplitude up to  $z \sim 3$ , consistent with available observational evidence.

**Key words.** galaxies: formation – galaxies: evolution – galaxies: star formation – galaxies: statistics – galaxies: stellar content

## 1. Introduction

The evolution of the large-scale spatial distribution of galaxies along cosmic epochs, i.e. the so-called Large Scale Structure (LSS) of the Universe, provides one of the most powerful constraints in observational cosmology. Galaxy surveys (see, e.g., Sánchez et al. 2006) have also shown the relevance of galaxy correlation functions, and in particular the two-point correlation function (2pCF), as a useful statistical estimator to characterize the LSS. The redshift evolution of galaxy 2pCF seems to be weaker/slower than the expected evolution of the clustering for the underlying mass distribution in concordance cosmologies (Jenkins et al. 1998): this mismatch is usually interpreted as the effect of physical mechanisms acting on the baryonic component. This implies that the redshift evolution of the 2pCF can also provide important constraints for baryon physics and galaxy formation models. Indeed, successful theoretical models of galaxy evolution on cosmological volumes usually aim to reproduce the redshift evolution of key statistical estimators, which are revealing of the correct build up of the stellar mass ( $M_*$ ) as a function

of redshift, like the galaxy stellar mass function (GSMFs) or luminosity functions (LFs). Nonetheless, it is also of fundamental importance that these models are able to correctly describe how the different galaxy types populated host dark matter (DM) haloes (and sub-haloes) in different density environments (see, e.g., Cole & Kaiser 1989).

According to the classical interpretation of the 2pCF shape, it can be seen as a combination of (see, e.g., Cooray & Sheth 2002): a 2-halo term - corresponding to pairs of galaxies belonging to independent halos - and a 1-halo term - coming from pairs of galaxies living in the same halo. The 2-halo term is dominant at large scales (separations larger than  $\sim 3 \text{ Mpc}$ ) and comes mainly from pairs of central galaxies. The 1-halo term is responsible for the 2pCF shape at  $\lesssim 2 \text{ Mpc}$  and it is statistically dominated by galaxy pairs belonging to the same halo (that is at least one of the two galaxies is a satellite). Overall, the largest contribution to the global 2pCF comes from galaxies around the knee of the GSMF, i.e. with stellar masses similar to the Milky-Way (Li & White 2009). The small scale clustering is particularly sensitive to the number and distribution of satellite galaxies inside massive DMHs. Therefore, it provides important constraints to theoretical models of galaxy formation, as it critically

\* e-mail:fabio.fontanot@inaf.it

depends on the treatment adopted for satellite galaxies and in particular their survival times. Therefore, it can be significantly affected by numerical resolution effects (Guo & White 2014).

Observationally, only the projected 2pCF -  $w(r_p)$  - is directly accessible, while the tridimensional 2pCF can be recovered via de-projection. Early results by Davis & Geller (1976) already showed a clear dependence of clustering amplitude with galaxy type, by showing that early type galaxies are more clustered than late-type galaxies. The advent of large area redshift surveys like the Sloan Digital Sky Survey (SDSS) provided the statistics to explore the dependence of  $w(r_p)$  amplitude and shape on galaxy properties such as luminosity (see, e.g., Zehavi et al. 2002) or stellar mass (Li et al. 2006), showing that brighter/more massive galaxies are more clustered than their fainter/less massive counterparts. A stronger difference in the clustering signal is found when considering galaxies of different colour (see, e.g., Li et al. 2006); at fixed  $M_*$  (or luminosity), red galaxies sensibly more clustered than blue galaxies. Galaxy colour is sensitive to the star formation rate (SFR) of model galaxies, which is regulated by a complex network of internal and external physical mechanisms. Therefore, clustering predictions for the active and passive galaxy populations represent an additional diagnostic to assess whether a given model reproduces the observational data in terms of star formation quenching as a function of the environment.

These results have been then confirmed and extended to higher redshift, thanks to redshift surveys such as the Galaxy And Mass Assembly (GAMA), VIMOS<sup>1</sup> Public Extragalactic Redshift Survey (VIPERS), the VIMOS-VLT Deep Survey (VVDS), the VIMOS Ultra Deep Survey (VUDS), the Deep Extragalactic Evolutionary Probe (DEEP2), the spectroscopic redshift Cosmic Evolution Survey (zCOSMOS) and showing that these conclusions generally hold up to  $z \sim 1$  (see, among others, Coil et al. 2006; Pollo et al. 2006; Meneux et al. 2008, 2009; Marulli et al. 2013; Skibba et al. 2014; Farrow et al. 2015; Coil et al. 2017) and providing the first estimates of the 2pCF at  $z \gtrsim 2$  (Durkalec et al. 2018). Overall, there is still some debate about the redshift evolution of the amplitude of the 2pCF: results from DEEP2 and VVDS favour a small evolution of clustering amplitude with redshift, while VIPERS and zCOSMOS show negligible differences with respect to  $z \sim 0$ . It worth stressing the difficulties in comparing clustering measurements at different redshift, due to the different galaxy selection biases reflecting in the sampling of the different galaxy population. Moreover, the difference in clustering amplitudes of active and passive galaxies has been confirmed out to  $z \sim 2$ : Coil et al. (2017) studied the clustering as a function of SFR, and they found the same trends defined by colours at low- $z$ , galaxies below the star-forming main sequence are more clustered than galaxies above it (see also Mostek et al. 2013).

In this paper, we exploit predictions from the latest version of the GALaxy Evolution and Assembly (GAEA), that couples an explicit partitioning of the cold gas into its molecular and neutral phases with an improved modelling of both cold gas accretion onto central Super-Massive Black Holes (SMBHs), and gas stripping in dense environments. We showed in our recent work (De Lucia et al. 2024; Xie et al. 2024) that this model realization correctly reproduces the observed fractions of quenched galaxies up to  $z \sim 3-4$ , while predicting number densities of massive quiescent galaxies at  $z \sim 3$  that are the largest among recently published models. We will thus take advantage of the most recent determinations for the 2pCF at several redshifts to assess if our model

is also able to reproduce both the global spatial distribution of galaxies in the LSS, and the distribution of galaxy populations split by their star formation activity. The latter test will represent a critical confirmation of the activity of GAEA to correctly grasp the physical mechanisms responsible for the regulation of star formation in galaxies.

Most of our previous GAEA realizations have been run on dark matter merger trees extracted from the Millennium Simulation (Springel et al. 2005, MS hereafter). This realization is based on a cosmological model whose parameters are offset with respect to more recent measurements – particularly for the normalisation of the density fluctuations at the present day ( $\sigma_8$ ) and  $\Omega_m$ . In this paper, we will introduce a novel GAEA realization, run on the P-MILLENNIUM simulation (Baugh et al. 2019, PMS hereafter), featuring a bigger cosmological volume, an updated cosmology, a better mass resolution and a finer time sampling. In particular, we will discuss the redshift evolution of key statistical quantities like the GSMFs or the AGN LFs as well as of galaxy clustering, as a function of stellar mass and star formation activity.

This paper is organized as follows. In Section 2 we will present the new GAEA realization run on merger trees extracted from the PMS simulation. In Section 3 we compare these predictions with previous realizations of the same model run on different cosmological simulations. In Section 4 we discuss the predicted clustering of model galaxies at different redshift and as a function of different galaxy properties. Finally, we present and discuss our conclusions in Section 5.

## 2. N-body simulations and the galaxy formation model

### 2.1. Numerical Simulations

In this work, we will focus on predictions from a GAEA realization coupled with merger trees extracted from the P-MILLENNIUM N-body simulation Baugh et al. (PMS 2019). Moreover, we will compare our results against predictions from two other GAEA runs, based on the MILLENNIUM Simulation (Springel et al. 2005, MS) and MILLENNIUM II Simulation (Boylan-Kolchin et al. 2009, MSII). These runs corresponds to the predictions at the basis of our recent work (De Lucia et al. 2024; Xie et al. 2024). Details on the assumed cosmologies, box size and particle resolution for each N-body simulation are listed in Table 1.

The PMS follows the evolution of the matter distribution in a volume of  $800^3 \text{ Mpc}^3$ , employing roughly 128 billion particles to trace the assembly of the Dark Matter Haloes (DMHs). In terms of mass resolution ( $m_p = 1.06 \times 10^8 h^{-1} M_\odot$ ), the PMS provides intermediate results to the MS and MSII. Moreover, it also provides an updated cosmology, based on the first year results from the Planck satellite (Planck Collaboration XVI 2014), with respect to the MS and MSII, that were run assuming cosmological parameters consistent with first year results of the WMAP satellite (Spergel et al. 2003).

The initial conditions for the PMS have been generated at  $z=127$  using second order Lagrangian perturbation theory (see Jenkins 2013, for more details), and the simulation has been run using a reduced memory version of the N-body code GADGET (Springel et al. 2005). Halo and Sub-Halo catalogues have been extracted on the fly using a classical FOF algorithm and the substructure finder code SUBFIND (Springel et al. 2001): halos and sub-haloes information have been saved on a regular grid of 271 output times (i.e. snapshots), equally spaced in expansion factor. This has to be compared with the 64-68 snapshots of the MS and MSII over the same redshift range. The gain in temporal

<sup>1</sup> Visible Multi Object Spectrograph

**Table 1.** Cosmological parameters for the simulations considered in this work:  $\sigma_8$  the normalisation of the density fluctuations at the present day;  $H_0$  the Hubble constant (in units [ $\text{km s}^{-1} \text{Mpc}^{-1}$ ]);  $n_{\text{spec}}$  is the spectral index of the primordial density fluctuations;  $L_{\text{box}}$  the simulation box length (in units [ $(h^{-1} \text{Mpc})$ ]);  $N_p$  the number of particles,  $M_p$  the particle mass (in units [ $h^{-1} M_\odot$ ]).

	$\Omega_b$	$\Omega_m$	$\Omega_b$	$\sigma_8$	$n_{\text{spec}}$	$H_0$	$L_{\text{box}}$	$N_p$	$\text{Log}(M_p)$
MS	0.75	0.25	0.0455	0.9	1.0	73	500	$2160^3$	8.935
MSII	0.75	0.25	0.0455	0.9	1.0	73	100	$2160^3$	6.838
PMS	0.693	0.307	0.04825	0.8288	0.9611	67.77	542.16	$5040^3$	8.025

**Table 2.** Parameter Calibration chart. The value of the parameters are identical in all runs presented in this paper.

Parameter	Value	Meaning
$\alpha_{\text{SF}}$		Star Formation efficiency
$\epsilon_{\text{reheat}}$	0.13	Reheating efficiency
$\epsilon_{\text{eject}}$	0.10	Ejection efficiency
$\gamma_{\text{reinc}}$	0.68	Reincorporation efficiency
$\kappa_{\text{radio}}/10^{-5}$	0.6	Hot gas Black Hole accretion efficiency
$f_{\text{lowJ}}/10^{-3}$	6.0	Cold gas angular momentum loss efficiency
$f_{\text{BH}}/10^{-3}$	0.09	Black hole accretion rate from reservoir
$\epsilon_{\text{qw}}/10^2$	3.2	Quasar wind efficiency
$f_{\text{cen}}/10^{-3}$	3.0	fraction of ISM added to the BH reservoir as a consequence of AGN-driven outflows
$\text{rp}_{\text{time}}$	400	Timescale of hot gas ram-pressure stripping
$\text{kesi}_{\text{slow}}$	1.4	Ratio between specific angular momentum of gas cooling through ‘slow mode’ and that of the halo
$\text{kesi}_{\text{rapid}}$	3.0	Ratio between specific angular momentum of gas cooling through ‘rapid mode’ and that of the halo

(redshift) resolution is particularly relevant at  $z \gtrsim 4$  where the PMS has  $\sim 100$  snapshots against the  $\sim 25$  of the MS/MSII. In order to run GAEA on the PMS volume, we have constructed subhalo based merger trees using the same approach described in [Springel et al. \(2005\)](#). We refer to this paper for a detailed description of the algorithm. In summary, for any given subhalo, we identify a unique descendant by finding all subhalos at the subsequent output that contain its most bound particles. We then give higher weight to those particles that are more tightly bound to the subhalo under consideration, and select as descendant the subhalo containing a larger fraction of the most bound particles. In this way, we aim at tracing the fate of the inner regions of the substructure, that might survive for longer time after it has been accreted onto a larger structure. Following ([Springel et al. 2005](#)), we search for descendants in the two following outputs to deal with small subhalos that fluctuate below and above the assumed detection threshold (20 bound particles). Once a unique descendant has been identified for all subhalos in the simulated volume and for all available outputs, links to all progenitors are automatically established, and merger trees can be built. We adopt the same merger tree structure defined for the Millennium Simulation suite and shown in Fig. 11 of ([Springel et al. 2005](#)). The merger trees adopted in this work have been constructed using half of the available outputs. While reducing the number of redshifts available, this choice reduces the memory and computational requirements of our GAEA runs. In a forthcoming paper (Cantarella et al., in preparation), we will show that results are not significantly different from those obtained using merger trees constructed considering all available snapshots.

In Fig. 1 (left panel), we compare the DM halo mass functions (HMFs) derived from the `SUBFIND` subhalo group catalogues for the MS (shaded areas), MSII (dashed lines) and PMS (point with poissonian errorbars), in the redshift range  $0 < z < 5$ . The MS and MSII agree well over the mass range where both simulations have enough volume and resolution. On the other hand, the PMS shows less structures at high redshift and a faster evolution of the mass function, that is very close to that computed from the MS at  $z \sim 0$ . In order to understand the origin of these differences

we consider in Fig. 1 (right panel) the evolution of the HMF shape for varying cosmological parameters. We evaluate analytic fits to the HMF at  $3 < z < 5$  by assuming the [Tinker et al. \(2008\)](#) model and using the `HMFCAL` tool developed by [Murray et al. \(2013\)](#). In all panels, the dashed black lines refer to HMFs predicted assuming the MS cosmology. The red solid lines in the left panels correspond to HMFs in the PMS cosmology. In the other panels, we show the HMFs predicted by varying only a few selected parameters with respect to the MS cosmology. In particular we consider MS models with  $\sigma_8 = 0.8288$  (blue solid lines), with  $\sigma_8 = 0.8288$  and  $n_{\text{spec}} = 0.9611$  (cyan dotted lines), with  $\Omega_m = 0.307$  (green solid lines). This comparison highlights that the differences between MS and PMS are mainly driven by the lower value of  $\sigma_8$  used in PMS. The difference in  $n_{\text{spec}}$  and  $\Omega_m$  result in (smaller) opposite effects, enhancing and contrasting the trends induced by the different  $\sigma_8$ , respectively.

## 2.2. GAEA

In this study we consider predictions from our latest rendition of the GAEA semi-analytic model (SAM). The approach starts from a statistical description of the assembly of the Large Scale Structure (i.e. a merger tree) that can be either analytically derived or extracted from numerical experiments. Galaxies are assumed to form within DM haloes, under the effect of a complex network of physical processes responsible for energy and mass exchanges among different baryonic components. SAMs follow the evolution of galaxy populations by numerically solving a system of differential equations, aiming at describing specific physical mechanisms, using parametrizations derived from empirical, numerical or theoretical arguments. The parameters involved are calibrated against a well defined set of observational constraints, by sampling efficiently the parameter space. The main advantage of the SAM approach lies in its reduced computational demand, with respect to an hydro-dynamical simulations: they are an optimal tool for studying galaxy evolution over large cosmological volumes, with enough flexibility to extensively test different physical models, explore their associated parameter space, and

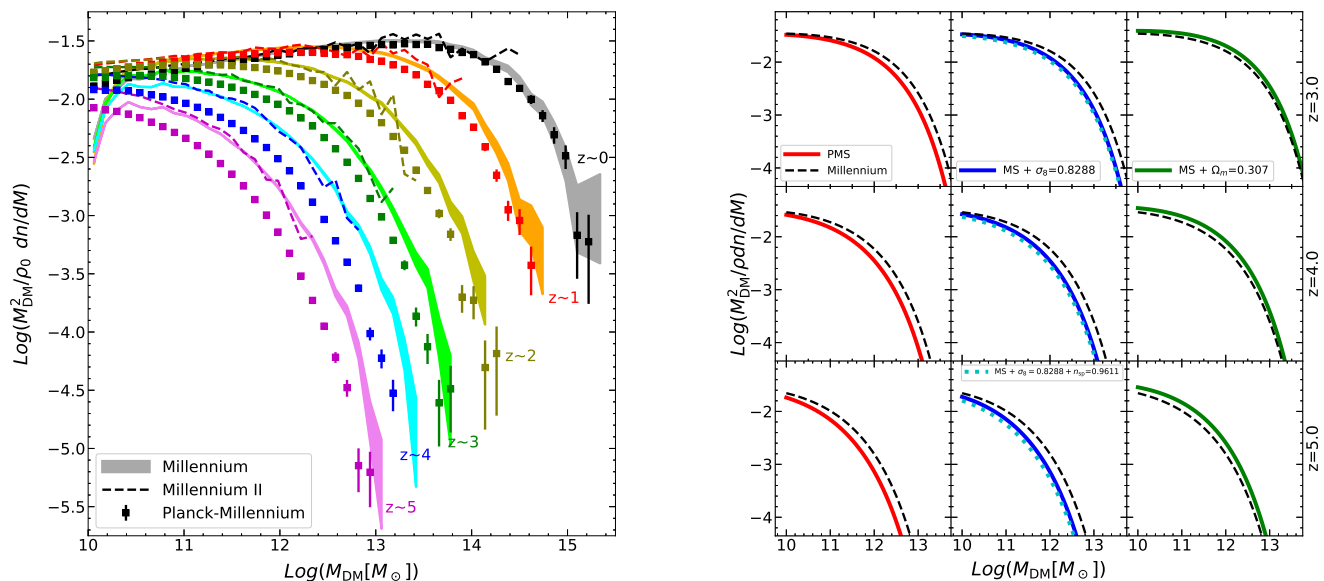


**Fig. 1.** *Left Figure:* Dark Matter HMF for the different simulations considered in this paper. Shaded regions show measurements based on the Millennium Simulation ( $1-\sigma$  poissonian scatter); dashed lines correspond to the Millennium II simulation and red squares with errorbars for the P-MILLENNIUM simulation ( $1-\sigma$  poissonian scatter). *Right Figure:* Impact of different cosmological parameters on the evolution of the HMF. The left-most panels show the HMFs expected for the MS and PMS cosmological models (dashed black and red solid lines respectively). In the central and right-most panels, the HMFs for the MS is compared with runs with theoretical expectations obtained modifying the following parameters:  $\sigma_8$  (assumed to be the same as in the PMS ; blue solid line);  $\sigma_8$  and the spectral index (as in the PMS ; cyan dotted line),  $\Omega_m$  (as in the PMS ; green solid line).

therefore the impact of individual physical mechanisms to set the observed properties of different galaxy populations.

GAEA builds from the model originally presented in De Lucia & Blaizot (2007), but now includes several improvements and further developments. In particular: (a) the modelling of chemical enrichment, based on a non-instantaneous treatment of the ejection of gas, metals and energy that accounts for the mass dependence of stellar lifetimes (De Lucia et al. 2014); (b) an improved treatment for stellar feedback, partially based on results of high-resolution hydrodynamical simulations (Hirschmann et al. 2016); (c) a detailed tracing of the evolution of angular momentum (Xie et al. 2017). The latest rendition of the model has been presented in De Lucia et al. (2024, DL24 hereafter) and merges independently developed versions, namely (d) the Xie et al. (2017) explicit partition of the cold gas into its atomic and molecular components; (e) the Xie et al. (2020) treatment for the non-instantaneous stripping of cold and hot gas in satellites galaxies; and (f) the Fontanot et al. (2020) modelling for cold gas accretion onto super-massive Black Holes (SMBH) and the onset of AGN-driven outflows. This new version of the GAEA model has been calibrated on the  $z < 3$  evolution of the galaxy stellar mass function (GSMF), on the  $z < 4$  evolution of the AGN luminosity function (LFs) and on the local HI and H2 mass function. DL24 shows that it correctly reproduces the evolution of the fraction and number densities of quenched galaxies up to  $z \sim 4$ , providing the largest number densities of massive galaxies at  $z > 3$  among similar theoretical models, predicting the rise of the first massive quenched galaxies at  $z \sim 6 - 7$  (Xie et al. 2024). A more throughout analysis of the properties of the highest- $z$  galaxies, especially in terms of their predicted UV luminosities as seen by JWST, will be presented in forthcoming work (Cantarella et al., in preparation). We stress that

the latest GAEA rendition preserves the good agreement with a variety of observational constraints that have been explored in recent years, such as the evolution of the mass-metallicity relations (Fontanot et al. 2021, both for the gaseous and stellar phases - see also Fig. A.5), the  $z > 3$  GSMF and the cosmic star formation rate density up to the highest redshifts for which observations are available (Fontanot et al. 2017).

### 3. Convergence of model predictions on different simulations

In order to appreciate the effect of a change in the cosmological parameters and resolution on the predictions of our model, we consider GAEA runs over merger trees extracted from the PMS, MS and MSII. All predictions we discuss in the following sections are based on model realization using the same values for the relevant physical parameters involved in the SAM definition. These parameters have been calibrated on the MS trees and correspond to the model presented in DL24. We list the most relevant in Table 2. In the following, we will show model predictions convolved with an estimated error on stellar and gaseous masses of 0.25 dex, thereby taking the Eddington bias (Jeffreys 1938; Eddington 1940) into account. The uncertainty considered represents a conservative choice especially at high- $z$ . We contrast model predictions from the different simulations with compilations of observational data used in our previous works. In this section (Fig. 2), we focus on a basic set of physical properties, whose evolution is crucial for understanding the process of galaxy assembly, like the Galaxy Stellar Mass Function (GSMF - left panel) from  $z \sim 0$  to  $z \sim 3$  and the AGN bolometric Luminosity Function (LF, right panel) from  $z \sim 0$  to  $z \sim 4$ . Those are among the main observables used to calibrate our model. In Appendix A,

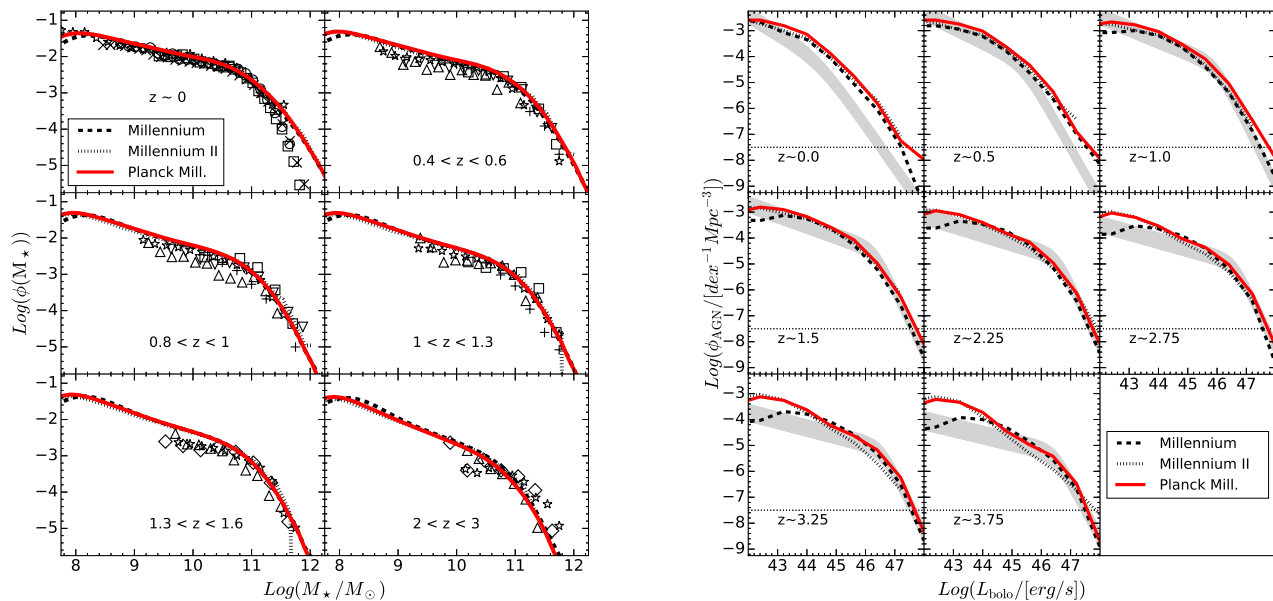


**Fig. 2.** *Left panel:* Redshift evolution of the galaxy stellar mass function ; datapoints correspond to the compilation used in Fontanot et al. (2009, see complete reference list for their Fig. 1). *Right panel:* Redshift evolution of the bolometric QSO/AGN-LF; the shaded regions show the expected space density from the empirical estimate of Shen et al. (2020). Black solid, black dashed and red solid lines refer the GAEA model version presented in De Lucia et al. (2024) and run on the Millennium, Millennium II and Planck Millennium simulations respectively.

we include additional observational constraints considered for model calibration, plus several predictions we consider in our recent work.

It is remarkable that predictions corresponding to realizations run on different simulations show such a high level of consistency. This shows that our latest rendition of the GAEA model exhibits an improved convergence with respect to previous versions. This is remarkable for the predicted evolution of the AGN-LF: the space density of faint AGNs is very sensible to the number of trigger events (i.e. mergers) and in the past this has limited the convergence of our model to relatively bright luminosities (see e.g. Fig. A2 in Fontanot et al. 2020). The latest GAEA version shows a good convergence between the MS and the PMS runs down to  $L_{\text{bolo}} \sim 10^{42}$  erg/s at  $z < 1$ , and down to  $L_{\text{bolo}} \sim 10^{44}$  erg/s at higher redshifts; predictions from the PMS and MSII agree even better around the knee of the LF, while at brighter luminosities, the MSII lacks volume to correctly reproduce the rarer sources. For all other statistical estimators the level of convergence between the different runs is high and in most cases predictions based on different simulations are virtually indistinguishable. We interpret this effect as a result of the interplay between the improved modelling of star formation, based on the partition of the cold gas as in Xie et al. (2017), and the new prescription for cold gas accretion onto the central SMBHs (Fontanot et al. 2020). Both physical mechanisms act as regulators of the total amount of cold gas available for star formation, chemical enrichment and SMBH accretion. In fact, versions of the model implementing just one of the two physical mechanisms (and run on different simulation) do not achieve the same level of convergence over such a wide range of redshift and physical properties, as that presented here.

## 4. Clustering Analysis

### 4.1. Redshift evolution of the 2-point correlation function

We then consider the predicted correlation functions for our model universes at different redshifts. In the following, we will focus on the projected 2-point correlation function  $w(r_p)$ ; this choice makes the comparison with observational data straightforward, and does not have to rely on de-projection algorithms. We study the evolution of the projected correlation function using estimates from several surveys: going from low- $z$  to higher redshifts we compare against results from SDSS (Li et al. 2006,  $z \sim 0.1$ ), GAMA (Farrow et al. 2015,  $z < 0.2$ ), VIPERS (Marulli et al. 2013,  $0.5 < z < 1.1$ ), DEEP2 (Li et al. 2006,  $z \sim 0.9$ ), VVDS (Meneux et al. 2008,  $z \sim 0.9$ ), zCOSMOS (zCOSMOS Meneux et al. 2009,  $z \sim 0.9$ ) and VUDS (Durkalec et al. 2018,  $z \sim 2.7$ ). We collect all these observational measurements in Fig. 3 and we contrast them with the prediction from GAEA realizations based on the MS (black dashed lines) or the PMS (red solid lines). We compute  $w(r_p)$  from GAEA using the python CORFUNC package (Sinha & Garrison 2020); model galaxy samples have been extracted from the simulated volumes considering all galaxies in the stellar mass range indicated in the legend, i.e. we do not attempt to replicate selection criteria specific of the different surveys considered. In our analysis we include an estimate for the typical error on  $M_*$  by convolving the intrinsic predictions of the model with a log-normal error distribution of amplitude 0.25 dex. We check that our main conclusions do not depend on this choice: as  $w(r_p)$  predictions based on intrinsic  $M_*$  provide a consistent picture.

Overall, the level of agreement between theoretical and observed correlation functions is impressive over the entire redshift range considered. Models run on the MS and PMS agree well with each other, but for a tendency of the MS runs to predict systematically stronger correlations. The effect is more pronounced

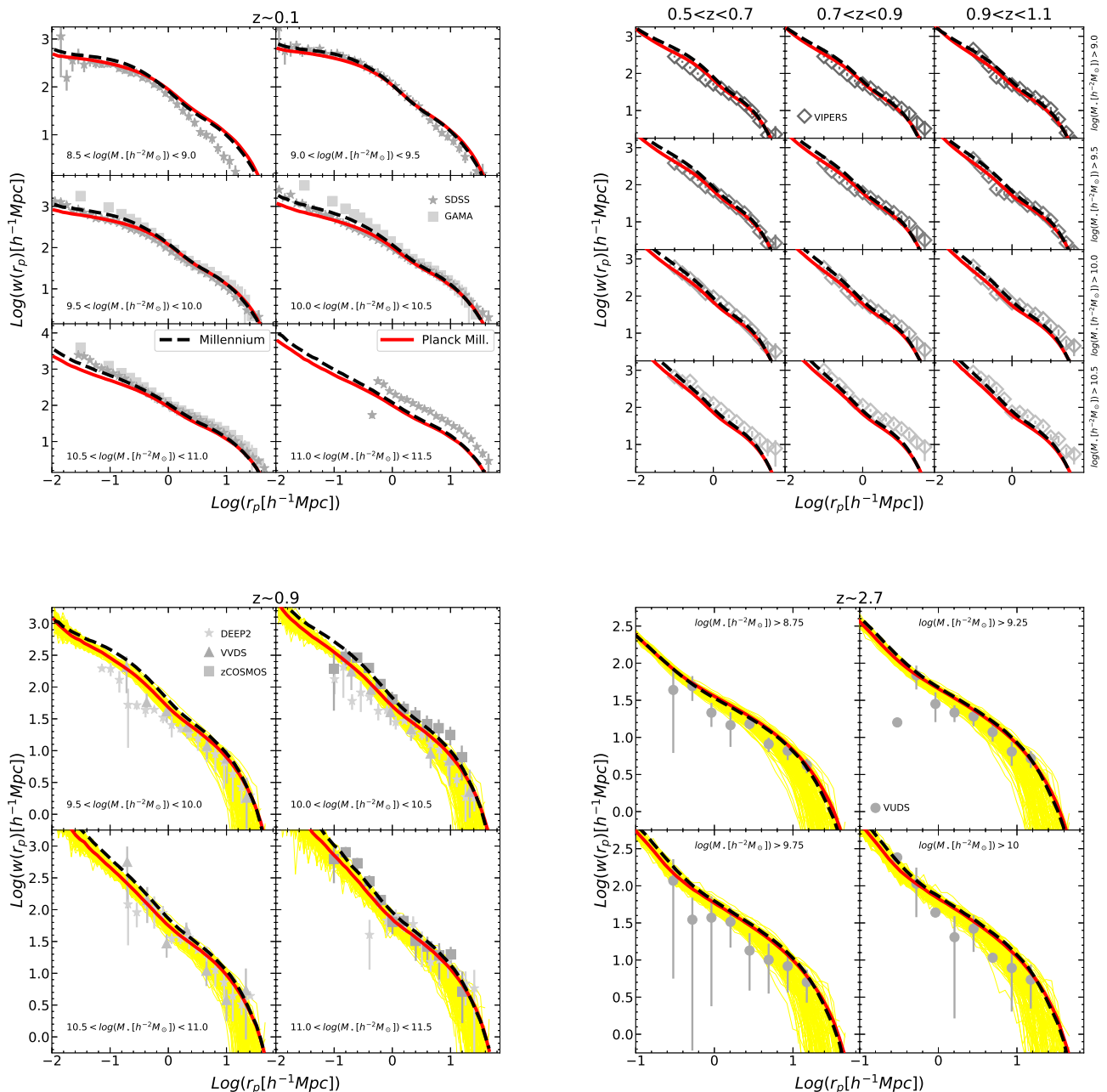


**Fig. 3.** Redshift evolution of the projected 2-point correlation function at different bins of stellar mass (as labelled). *Upper left panel:* data from SDSS at  $z \sim 0$  (Li et al. 2006). *Upper right panel:* data from VIPERS at  $0.5 < z < 1.1$  (Marulli et al. 2013). *Lower left panel:* data at  $z \sim 0.9$  from VVDS (Meneux et al. 2008), zCOSMOS (Meneux et al. 2009), DEEP2 obtained using the same techniques as in Li et al. (2006). *Lower right panel:* data from VUDS at  $2 < z < 3.5$  (Durkalec et al. 2018). GAEA predictions refer to the realizations run on the Millennium Simulation (black dashed line) and on the Planck Millennium Simulation (red solid line) as in Fig. 2. Yellow areas show the effect of cosmic variance (computed considering 125 independent subvolumes of the PMS - see text for more details).

at small stellar masses and close separations, and we ascribe it to the larger value of  $\sigma_8$  used in the MS. At  $z < 0.2$  (Fig. 3, upper left panel), theoretical  $w(r_p)$  are very close to SDSS constraints for  $M_\odot < 10^{11} M_\odot$ , but they tend to underestimate the correlation signal measured for more massive galaxies. Similar conclusions hold at intermediate redshifts ( $0.5 < z < 0.9$ ) for VIPERS (Fig. 3, upper right panel), but the underprediction in the highest mass bin reduces considerably as the redshift increases. The situation is slightly more complex at  $z \sim 0.9$ , where different

surveys suggest slightly different normalization for  $w(r_p)$ . This could be due to the different surveyed volume or to the presence of overdensities (like in the case of the zCOSMOS sample, (Meneux et al. 2009)). We explore the impact of cosmic variance by considering 125 independent and disjointed subvolumes in the PMS, and computing their corresponding 2pCF. The yellow areas in Fig. 3 highlight the range covered by these independent realizations: smaller  $w(r_p)$  amplitudes are indeed possible, especially at the largest separations. Nonetheless, GAEA predic-

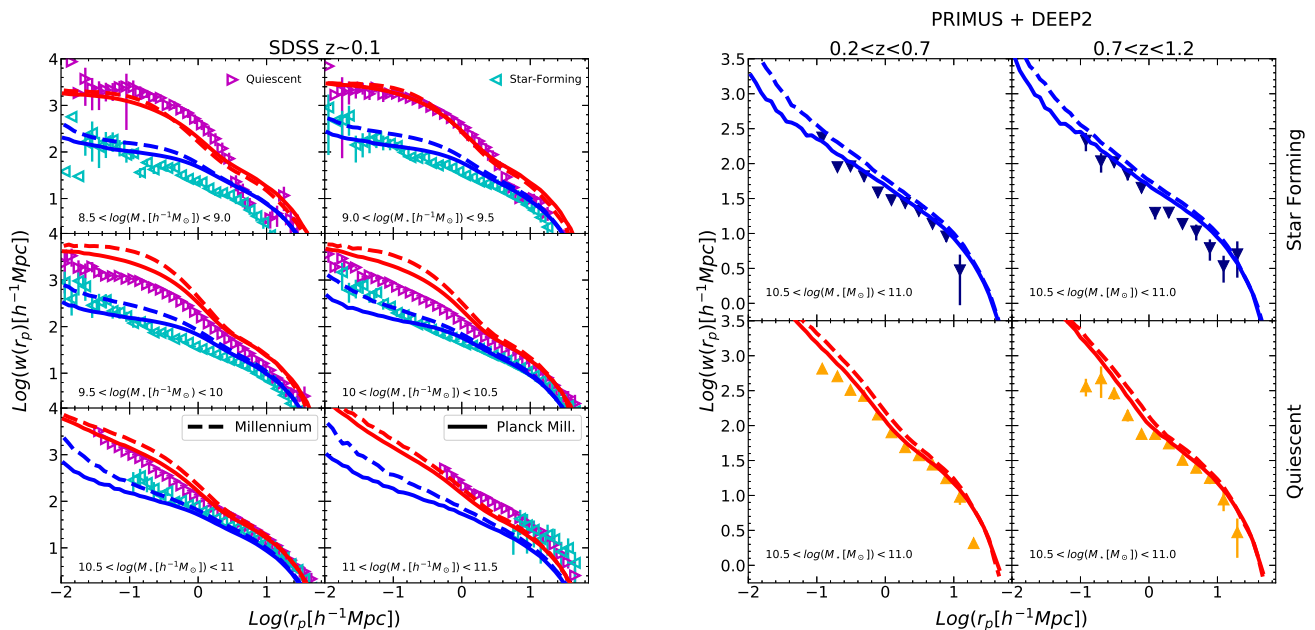


**Fig. 4.** *Left panel* Projected 2-point correlation function for red/blue galaxies at  $z \sim 0.1$ ; data from [Li et al. \(2006\)](#). *Right panel* Projected 2-point correlation function for star forming/quiescent galaxies; data from [Coil et al. \(2017\)](#). GAEA predictions refer to the realizations run on the Millennium Simulation (black dashed line) and on the Planck Millennium Simulation (red solid line) as in [Fig. 2](#).

tions lie within the clustering measurements obtained from different surveys at  $z \sim 0.9$  ([Fig. 3](#), lower left panel) and the agreement with data is good to the smallest separations measured. The predicted evolution of the  $w(r_p)$  normalization at  $z \lesssim 1$  is rather small: in most cases  $w(r_p)$  can be well approximated by a single power law over a wide separation scale; GAEA also reproduces the observed flattening of the relation at low- $z$  for the smallest separations probed by the SDSS. Moving to higher redshifts ( $2 < z < 3.5$ ), a larger difference in the  $w(r_p)$  normalization can be appreciated with respect to the VUDS data ([Fig. 3](#), lower right panel): uncertainties in the observational determination are typically larger than at lower redshift, and GAEA predictions are still consistent, although systematically larger, than the data. Cosmic variance can also have a large impact here (the VUDS volume correspond to  $\sim 1.75 \times 10^7 \text{ Mpc}^3$ , to be compared with the  $\sim 4 \times 10^6 \text{ Mpc}^3$  of the PMS subvolumes). We thus conclude that GAEA is able to correctly capture the observed evolution of the correlation strength up to  $z \lesssim 3.5$ : this represents a major success for our latest GAEA model release.

#### 4.2. Colour/SFR dependence of the 2-point correlation function

As we already discussed, several authors (see e.g. [Wang et al. 2013](#)) pointed out that the clustering strength depends not only on  $M_*$ , but also on the star formation activity of galaxy population, with red and quiescent galaxies being more clustered than their blue and star forming counterparts with similar  $M_*$ . In [Fig. 4](#), we compare model predictions with SDSS data at  $z \sim 0.1$  ([Li et al. 2006](#)) and data at  $z \sim 0.9$  ([Coil et al. 2017](#)) obtained combining the PRIMUS MULTI-object Survey (PRIMUS [Coil et al. 2011](#)) with DEEP2. At both redshifts we consider model predictions corresponding to quiescent and star-forming subsamples, using separation thresholds based on their specific SFR ( $s\text{SFR} = \text{SFR}/M_*$ ), for consistency with our previous work

([De Lucia et al. 2024](#)). At  $z \sim 0.1$ , model galaxies are classified using a  $s\text{SFR} = 10^{-11} \text{ yrs}^{-1}$  separation. This is formally different than the choice for SDSS galaxies, which have been split according to their g-r colour: however, we checked that using a classifications based on galaxy colours (e.g. as in [Springel et al. 2018](#)) does not qualitatively change our main results: GAEA realization reproduces well the stronger clustering of red galaxies with respect to blue sources, and in particular the relative clustering amplitudes between the two populations. Models over-predict the clustering strength for red galaxies at intermediate masses, irrespectively of the assumed cosmology. Overall, the clustering strength of blue galaxies is better reproduced over the entire mass range considered. At large masses, the model under-predict the observed clustering signal, but the relative clustering between the red and blue population is still well represented. At higher redshift, we contrast clustering estimates from the PRIMUS and DEEP2 surveys with GAEA predictions by splitting model galaxies into a quiescent and star forming subsamples, using the same (redshift-dependent)  $s\text{SFR}$  threshold employed in the data ([Coil et al. 2017](#)):

$$\log \text{SFR} = -1.29 + 0.65 \times (\log M_* - 10) + 1.33(z - 0.1) \quad (1)$$

The agreement between data and model prediction in the single mass bin available ( $10.5 < \text{Log}(M_* [h^{-1} M_\odot]) < 11$ ) is very good, both for the red and blue populations. Overall, the results presented in [Fig. 4](#) indicate that the treatment for physical mechanism responsible for quenching in GAEA correctly reproduces not only the overall assembly and evolution of the quenched galaxy population ([De Lucia et al. 2024](#); [Xie et al. 2024](#)), but also their spatial distribution in the cosmic web. This confirms that the model correctly capture the relative role of internal and environmental processes in shaping the galaxy properties in different environments.

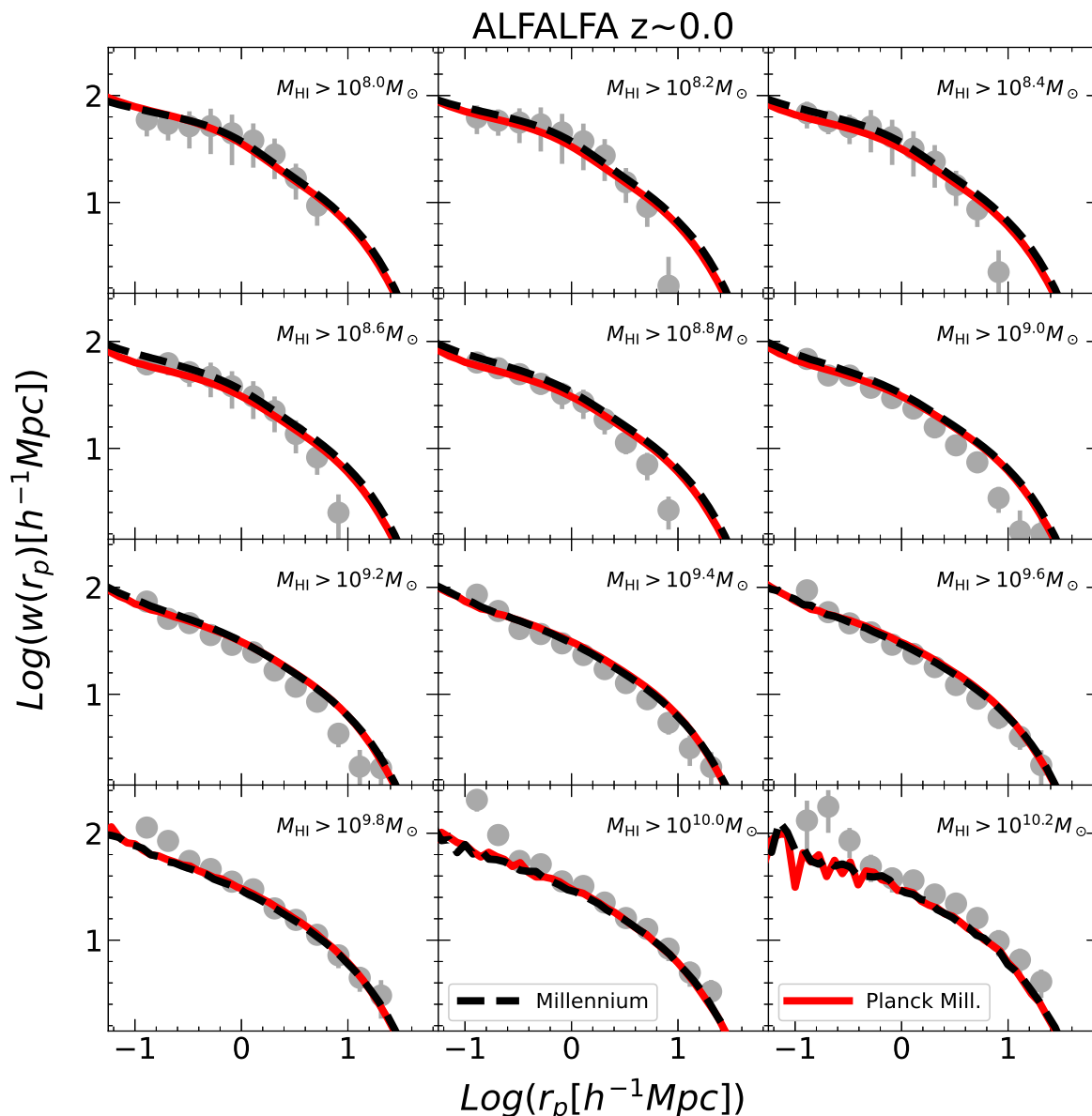


**Fig. 5.** Projected 2-point correlation function for HI selected galaxies  $z \lesssim 0.05$ ; data from Guo et al. (2017). GAEA predictions refer to the realizations run on the Millennium Simulation (black dashed line) and on the Planck Millennium Simulation (red solid line) as in Fig. 2.

#### 4.3. 2-point correlation function for HI selected galaxies

In the previous sections, we study the 2pCF of galaxies selected on the basis of their stellar content. A complementary analysis involves the study of the cold gas content of galaxies, through the distribution of HI selected galaxies. Gas distribution in galaxies at low redshift can be mapped using the 21 cm HI hyperfine emission line. In particular, the Arecibo Fast Legacy ALFA Survey (ALFALFA; Giovanelli et al. 2005) samples more than 5000 galaxies out to  $z \sim 0.05$ , enabling the study of their clustering properties Papastergis et al. (2013), showed that HI selected galaxies exhibit a lower  $w(r_p)$  amplitude with respect to stellar mass selected samples. Guo et al. (2017) used the 70% complete

ALFALFA catalogue and showed that the 2pCF of HI-selected galaxies depends strongly on the HI mass, i.e. galaxies with higher HI reservoirs are more strongly clustered on scales above a few Mpc than their counterparts with lower HI content. We compare Guo et al. (2017) estimates at different HI-mass ( $M_{\text{HI}}$ ) thresholds with GAEA predictions in Fig. 5; we find a general good agreement in the clustering amplitude and, most importantly, in its relative evolution as a function of  $M_{\text{HI}}$ . The larger discrepancies are seen at the high- $M_{\text{HI}}$  end, although data and predictions are consistent within the statistical errorbars. This result is similar to those based on  $M_{\star}$  selected galaxies, although the reference samples refer to different model galaxy populations, as most massive galaxies at  $z \sim 0$  in GAEA have low gas fractions.



## 5. Discussion and conclusions

In this paper, we present predictions of the latest version of the GAEA model, run on merger trees extracted from the P-MILLENNIUM simulation. We compare model results against a compilation of observational measurements of galaxy clustering as a function of stellar mass and star formation rate, covering a wide redshift range from the local Universe up to the highest redshift when this measurement has been possible (i.e.  $z \sim 3.5$ ). Our model shows a satisfactory agreement with the observed projected 2pCF, of comparable or superior quality with respect to independent semi-analytic codes (L-GALAXIES Guo et al. 2011; Henriques et al. 2017) and hydro-dynamical simulations (Springel et al. 2018; Artale et al. 2017). At  $z \sim 0$ , GAEA results are close to those predicted from the TNG hydro-simulation suite (Springel et al. 2018): a good agreement with data is found at intermediate-to-low stellar mass bins and at the smallest scales, while the 2pCF in the highest mass bin has a smaller amplitude with respect to observational estimates. Similar results have been also found for predictions from the EAGLE simulation (Artale et al. 2017). Predictions from the L-GALAXIES model are able to better reproduce the  $w(r_p)$  amplitude in the highest-mass bin, but they either overpredict (Guo et al. 2011) or underpredict (Henriques et al. 2017) the clustering of intermediate-to-low mass galaxies. Overall, our model does not predict a significant evolution of the clustering strength with redshift, in good agreement with independent theoretical predictions (Artale et al. 2017) and observational measurements up to  $z \sim 1$  (Marulli et al. 2013). At higher redshift, data seem to suggest a more significant evolution of the clustering amplitude than model predictions, although these are still in agreement with data within  $1-\sigma$  error-bars and cosmic variance in the observed samples might play a relevant role. More data at  $z \gtrsim 2$  are definitely needed to clarify if the discrepancy between available measurements and model predictions is significant.

We estimate the clustering length  $r_0$  corresponding to our mock samples, by considering the value corresponding to a 2pCF  $\xi(r_0) = 1$ . GAEA predicts  $r_0$  values in the range  $\sim 4$  to  $\sim 6$   $h^{-1}$  Mpc, mildly increasing with stellar mass. These values are in good agreement with observational constraints for intermediate-to-low mass galaxies (see e.g. Foucaud et al. 2010; Wake et al. 2011; Lin et al. 2012), but underestimate the expected values at  $M_\star > 10^{11} h^{-1} M_\odot$  (typically larger than  $10 h^{-1}$  Mpc). This is a reflection of the underestimate of the clustering amplitude in the most massive stellar mass bin that we discussed in Sec. 4. At fixed stellar mass, we find only a weak evolution of  $r_0$  with redshift, in agreement with the numerical results from Artale et al. (2017).

If we split our model galaxies in star-forming and quiescent samples, we find that GAEA correctly reproduces the increased clustering of red quiescent galaxies with respect to blue star forming systems. At  $M_\star < 10^{11} h^{-1} M_\odot$ , the agreement with data for the blue population is excellent, while red galaxies show a clustering excess at intermediate stellar masses. This shows that the modelling of physical mechanisms responsible for quenching in GAEA (both internal and environmental) is able to reproduce the observed clustering strength and its variation with stellar mass. This is not a trivial success for our model, and it shows that our approach is not only able to recover the global properties of galaxy populations in a statistical sense, but also their spatial distribution in the LSS. For the most massive galaxies (larger than  $10^{11} h^{-1} M_\odot$ ), both the clustering amplitude of the quiescent and star-forming populations are underestimated. This

is consistent with the underestimate we find for the total population, and represents the main tension we found.

Most of the model galaxies contributing to the most massive bin are central galaxies. The underprediction of clustering amplitude for these galaxies highlights a mismatch between the predicted and expected mass of the host DMHs: GAEA galaxies tend to live in DMHs slightly less massive than what suggested by the clustering analysis. On the other hand, at low-stellar masses, that are dominated by the satellite population, the good agreement between data and predictions for the 1-halo term (i.e. at scales  $\lesssim 2-3$  Mpc) suggests that the satellite distribution within halos is correctly reproduced. This implies that our treatment for the evolution of satellite galaxies as in Xie et al. (2020) is effective in recovering the main properties of this population, both in terms of stellar mass and star formation activity. Conversely, the excess of clustering signal at low-masses for the 2-halo term (i.e. at scales  $\gtrsim 2-3$  Mpc) suggest that GAEA is predicting a larger than expected number of satellites in massive haloes: this can be related to our treatment of the merging times for orphan galaxies (i.e. satellite galaxies whose substructure has fallen below the resolution limit of the simulation).

In summary, the latest GAEA version shows a remarkable level of agreement for model predictions run on mergers trees extracted from simulation of different resolution and (slightly) different  $\Lambda$ CDM cosmological parameters. This result is driven by the interplay between the new treatment for AGN (and its feedback on the host galaxies) and the explicit partitioning of cold gas into its atomic and molecular components. Both physical mechanisms act as regulators of the cold gas in model galaxies. GAEA reproduces well the observed dependence of galaxy clustering on stellar mass and star formation activity. Moreover, model predictions are also consistent with the clustering measurements corresponding to HI-selected galaxies. This is an important confirmation that our treatment of the mechanisms acting on the baryonic component of galaxies, and satellites in particular, is able to capture the relevant physical dependencies. GAEA predicts a small redshift evolution of the amplitude of the 2pCF: this is consistent with available data up to  $z \sim 3.5$ , which we interpret as another indication that our model is able to correctly connect galaxies with their environment. At higher redshifts, our model tends to under-predict the observational measurements. However, cosmic variance may play an important role at these redshifts and larger observational samples are needed to draw firmer conclusions in this redshift regime.

*Acknowledgements.* An introduction to GAEA, a list of our recent work, as well as datafile containing published model predictions, can be found at <https://sites.google.com/inaf.it/gaea/home>. We acknowledge the use of INAF-OATs computational resources within the framework of the CHIPP project (Taffoni et al. 2020) and the INAF PLEIADI program (<http://www.pleiadi.inaf.it>). This work used the DiRAC@Durham facility managed by the Institute for Computational Cosmology on behalf of the STFC DiRAC HPC Facility ([www.dirac.ac.uk](http://www.dirac.ac.uk)). The equipment was funded by BEIS capital funding via STFC capital grants ST/P002293/1, ST/R002371/1 and ST/S002502/1, Durham University and STFC operations grant ST/R000832/1. DiRAC is part of the National e-Infrastructure. We thank Chen Li for sharing his observational estimates for the clustering signal in the SDSS and DEEP2 surveys. We acknowledge stimulating discussions with Andrea Biviano, Pierluigi Monaco and Emiliano Sefusatti. MH acknowledges funding from the Swiss National Science Foundation (SNSF) via a PRIMA grant PR00P2-193577 ‘From cosmic dawn to high noon: the role of BHs for young galaxies’.

## References

- Artale, M. C., Pedrosa, S. E., Trayford, J. W., et al. 2017, MNRAS, 470, 1771  
 Baugh, C. M., Gonzalez-Perez, V., Lagos, C. D. P., et al. 2019, MNRAS, 483, 4922

- Boylan-Kolchin, M., Springel, V., White, S. D. M., Jenkins, A., & Lemson, G. 2009, *MNRAS*, 398, 1150
- Coil, A. L., Blanton, M. R., Burles, S. M., et al. 2011, *ApJ*, 741, 8
- Coil, A. L., Mendez, A. J., Eisenstein, D. J., & Moustakas, J. 2017, *ApJ*, 838, 87
- Coil, A. L., Newman, J. A., Cooper, M. C., et al. 2006, *ApJ*, 644, 671
- Cole, S. & Kaiser, N. 1989, *MNRAS*, 237, 1127
- Cooray, A. & Sheth, R. 2002, *Phys. Rep.*, 372, 1
- Davis, M. & Geller, M. J. 1976, *ApJ*, 208, 13
- De Lucia, G. & Blaizot, J. 2007, *MNRAS*, 375, 2
- De Lucia, G., Fontanot, F., Xie, L., & Hirschmann, M. 2024, *A&A*, 687, A68
- De Lucia, G., Tornatore, L., Frenk, C. S., et al. 2014, *MNRAS*, 445, 970
- Durkalec, A., Le Fèvre, O., Pollo, A., et al. 2018, *A&A*, 612, A42
- Eddington, A. S., S. 1940, *MNRAS*, 100, 354
- Farrow, D. J., Cole, S., Norberg, P., et al. 2015, *MNRAS*, 454, 2120
- Fletcher, T. J., Saintonge, A., Soares, P. S., & Pontzen, A. 2021, *MNRAS*, 501, 411
- Fontanot, F., Calabrò, A., Talia, M., et al. 2021, *MNRAS*, 504, 4481
- Fontanot, F., De Lucia, G., Hirschmann, M., et al. 2020, *MNRAS*, 496, 3943
- Fontanot, F., De Lucia, G., Monaco, P., Somerville, R. S., & Santini, P. 2009, *MNRAS*, 397, 1776
- Fontanot, F., Hirschmann, M., & De Lucia, G. 2017, *ApJ*, 842, L14
- Foucaud, S., Conselice, C. J., Hartley, W. G., et al. 2010, *MNRAS*, 406, 147
- Giovanelli, R., Haynes, M. P., Kent, B. R., et al. 2005, *AJ*, 130, 2598
- Guo, H., Li, C., Zheng, Z., et al. 2017, *ApJ*, 846, 61
- Guo, Q. & White, S. 2014, *MNRAS*, 437, 3228
- Guo, Q., White, S., Boylan-Kolchin, M., et al. 2011, *MNRAS*, 413, 101
- Haynes, M. P., Giovanelli, R., Martin, A. M., et al. 2011, *AJ*, 142, 170
- Henriques, B. M. B., White, S. D. M., Thomas, P. A., et al. 2017, *MNRAS*, 469, 2626
- Hirschmann, M., De Lucia, G., & Fontanot, F. 2016, *MNRAS*, 461, 1760
- Jeffreys, H. 1938, *MNRAS*, 98, 190
- Jenkins, A. 2013, *MNRAS*, 434, 2094
- Jenkins, A., Frenk, C. S., Pearce, F. R., et al. 1998, *ApJ*, 499, 20
- Jones, M. G., Haynes, M. P., Giovanelli, R., & Moorman, C. 2018, *MNRAS*, 477, 2
- Keres, D., Yun, M. S., & Young, J. S. 2003, *ApJ*, 582, 659
- Kormendy, J. & Ho, L. C. 2013, *ARA&A*, 51, 511
- Li, C., Kauffmann, G., Jing, Y. P., et al. 2006, *MNRAS*, 368, 21
- Li, C. & White, S. D. M. 2009, *MNRAS*, 398, 2177
- Lin, L., Dickinson, M., Jian, H.-Y., et al. 2012, *ApJ*, 756, 71
- Marulli, F., Bolzonella, M., Branchini, E., et al. 2013, *A&A*, 557, A17
- McConnell, N. J. & Ma, C.-P. 2013, *ApJ*, 764, 184
- Meneux, B., Guzzo, L., de la Torre, S., et al. 2009, *A&A*, 505, 463
- Meneux, B., Guzzo, L., Garilli, B., et al. 2008, *A&A*, 478, 299
- Mostek, N., Coil, A. L., Cooper, M., et al. 2013, *ApJ*, 767, 89
- Murray, S. G., Power, C., & Robotham, A. S. G. 2013, *Astronomy and Computing*, 3, 23
- Papastergis, E., Giovanelli, R., Haynes, M. P., Rodríguez-Puebla, A., & Jones, M. G. 2013, *ApJ*, 776, 43
- Planck Collaboration XVI. 2014, *A&A*, 571, A16
- Pollo, A., Guzzo, L., Le Fèvre, O., et al. 2006, *A&A*, 451, 409
- Sánchez, A. G., Baugh, C. M., Percival, W. J., et al. 2006, *MNRAS*, 366, 189
- Shen, X., Hopkins, P. F., Faucher-Giguère, C.-A., et al. 2020, *MNRAS*, 495, 3252
- Sinha, M. & Garrison, L. H. 2020, *MNRAS*, 491, 3022
- Skibba, R. A., Smith, M. S. M., Coil, A. L., et al. 2014, *ApJ*, 784, 128
- Spergel, D. N., Verde, L., Peiris, H. V., et al. 2003, *ApJS*, 148, 175
- Springel, V., Pakmor, R., Pillepich, A., et al. 2018, *MNRAS*, 475, 676
- Springel, V., White, S. D. M., Jenkins, A., et al. 2005, *Nature*, 435, 629
- Springel, V., White, S. D. M., Tormen, G., & Kauffmann, G. 2001, *MNRAS*, 328, 726
- Taffoni, G., Becciani, U., Garilli, B., et al. 2020, *arXiv e-prints*, arXiv:2002.01283
- Tinker, J., Kravtsov, A. V., Klypin, A., et al. 2008, *ApJ*, 688, 709
- Wake, D. A., Whitaker, K. E., Labbé, I., et al. 2011, *ApJ*, 728, 46
- Wang, L., Weinmann, S. M., De Lucia, G., & Yang, X. 2013, *MNRAS*, 433, 515
- Xie, L., De Lucia, G., Fontanot, F., et al. 2024, *ApJ*, 966, L2
- Xie, L., De Lucia, G., Hirschmann, M., & Fontanot, F. 2020, *MNRAS*, 498, 4327
- Xie, L., De Lucia, G., Hirschmann, M., Fontanot, F., & Zoldan, A. 2017, *MNRAS*, 469, 968
- Zehavi, I., Blanton, M. R., Frieman, J. A., et al. 2002, *ApJ*, 571, 172
- Zwaan, M. A., Meyer, M. J., Staveley-Smith, L., & Webster, R. L. 2005, *MNRAS*, 359, L30

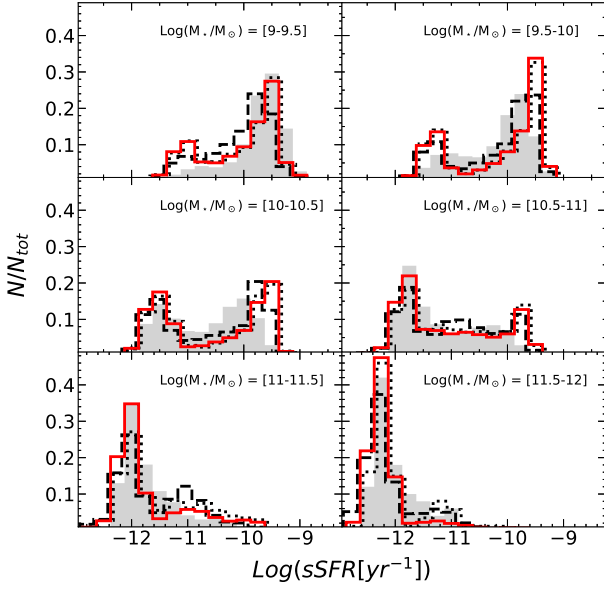


**Fig. A.1.** Specific star formation rate distribution in stellar mass bins, compared to SDSS DR8 observational estimates (grey shaded histograms). MS and MSII histograms have been slightly shifted (by 0.05 dex) for clarity. Black solid, black dashed and red solid lines refer the GAEGA model version presented in De Lucia et al. (2024) and run on the Millennium, Millennium II and Planck Millennium simulations respectively.

## Appendix A: Additional model predictions

In this Appendix we show additional observational constraints to further explore the convergence of the latest GAEGA model, and to demonstrate that our previously published results hold in the latest rendition of our model. We consider in Fig. A.1 the  $z \sim 0$  distribution of sSFR in stellar mass bins and in Fig. A.2 the evolution of the main sequence of star forming galaxies. In the latter figure, model star-forming galaxies have been selected as those with  $sSFR$  larger than  $0.3/t_H$ , where  $t_H$  is the Hubble time at the redshift under consideration. Fig. A.3 shows the  $z \sim 0$  scaling relation between the mass of the central SMBH ( $M_{BH}$ ) and the mass of the spheroidal component ( $M_{Bulge}$ ), while Fig. A.4 shows the gas-phase and stellar mass-metallicity relations. In Fig. A.5, we report the mass functions at  $z = 0$  for the neutral and molecular gas components. These distributions have been used for the calibration of the model on MS merger trees (Xie et al. 2017; De Lucia et al. 2024). Fig. A.5 shows that for the HI and H2 mass function the consistency between the model realizations run on different simulations is higher (i.e. it extends to smaller gas masses) than previous versions of the model (see e.g. Fig. 7 in Xie et al. 2017).

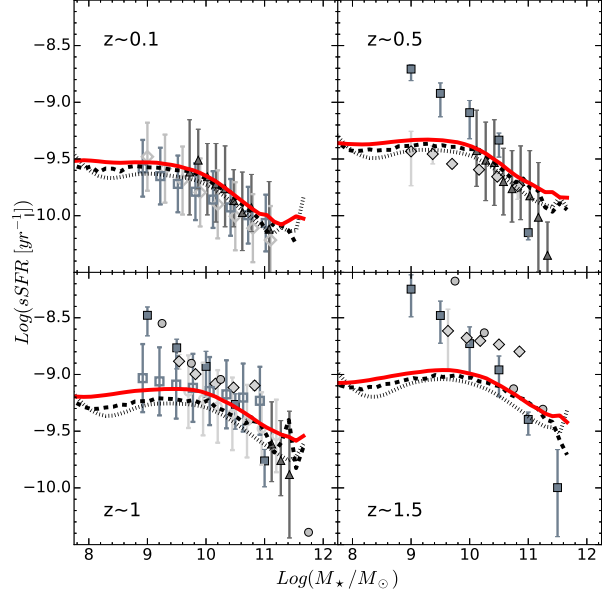


**Fig. A.2.** Redshift evolution of the main sequence of star-forming galaxies. Line-types and colours as in Fig. A.1, datapoints correspond to the compilations used in Fontanot et al. (2009, filled symbols, see complete reference list for their Fig. 5) and in Xie et al. (2017, empty symbols, see complete reference list for their Fig. 11).

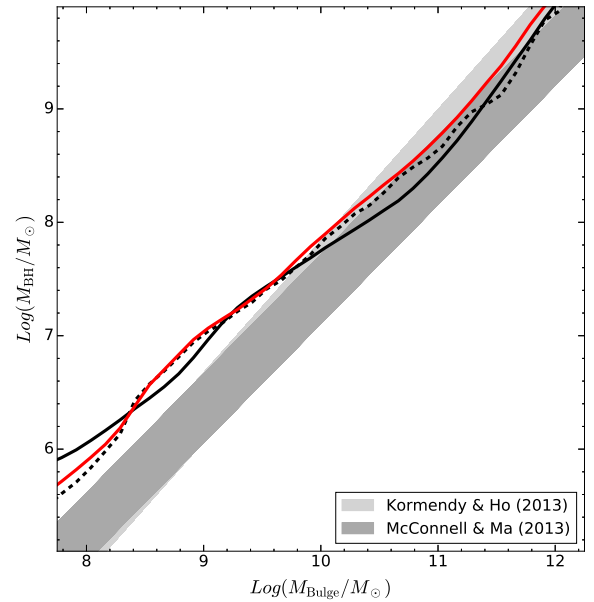


**Fig. A.3.**  $M_{BH}$ - $M_{Bulge}$  scaling relation at  $z \sim 0$ . Shaded areas correspond to the best fit relations of Kormendy & Ho (2013) and McConnell & Ma (2013), for both relations we assume a scatter of 0.3 dex. Line-types and colours as in Fig. A.1.

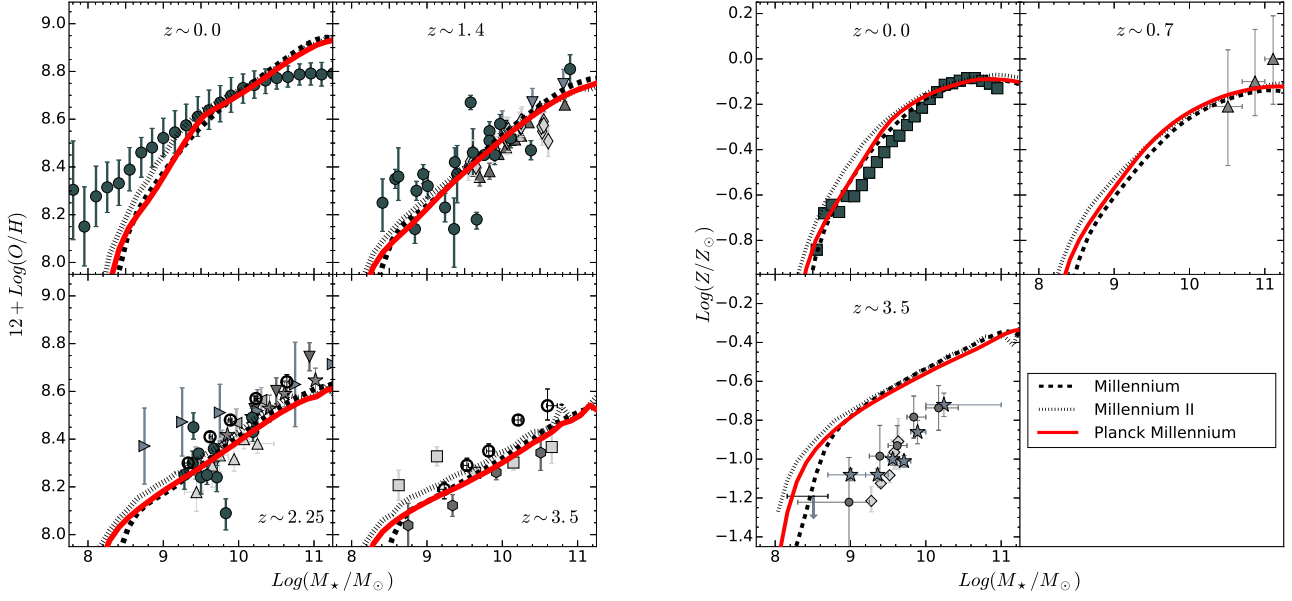


**Fig. A.4.** *Left panel:* Redshift evolution of the cold gas metallicity as a function of stellar mass (following Fontanot et al. 2021 we apply a downwards 0.1 dex shift to the intrinsic predictions). *Right panel:* stellar mass-metallicity relation at different redshifts. Line-types and colours as in Fig. A.1; in both panels datapoints correspond to the compilation used in Fontanot et al. (2021, see complete reference list for their Fig. 1).

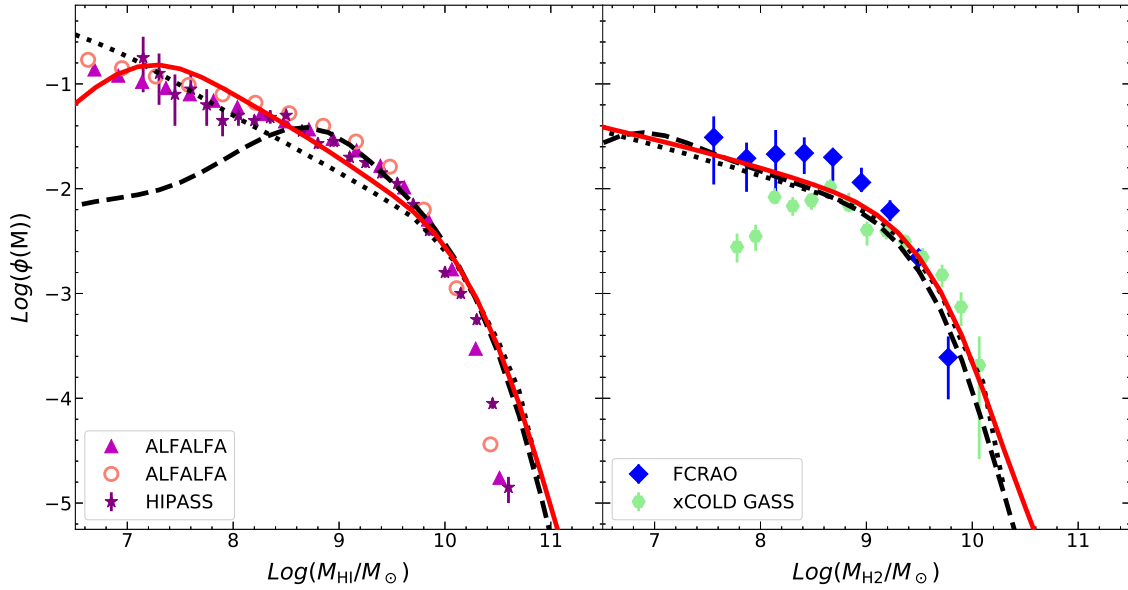


**Fig. A.5.** HI and H<sub>2</sub> mass functions at  $z \sim 0$  are shown in the left and right panel respectively. Observational data are from Keres et al. (2003, blue empty diamonds), Zwaan et al. (2005, purple stars), Haynes et al. (2011, magenta triangles), Jones et al. (2018, pink empty circles) and Fletcher et al. (2021, light green hexagons). Line-types and colours are as in Fig. A.1. Model predictions have been convolved with an estimated 0.25 dex error on the gas mass determination.